

ИНСТИТУТ ЗА ФИЗИКУ

Научном већу Института за физику у Београду

Београд, 25.7.2024.

ПРИМЉЕНО: 25. 07. 2024.			
Рад.јед.	б р о ј	Арх.шифра	Прилог
0801	1335/1		

Предмет:

Молба за покретање поступка за стицање звања истраживач-сарадник

На основу испуњености услова предвиђених Правилником о стицању истраживачких и научних звања, прописаног од стране ресорног Министарства, молим Научно веће института за физику у Београду да покрене поступак за мој избор у звање истраживач сарадник.

У прилогу достављам:

1. Мишљење руководиоца лабораторије са предлогом комисије за избор у звање
2. Стручну биографију
3. Преглед научне активности
4. Списак научних радова
5. Потврду о статусу студента докторских студија и пријављеној теми докторске дисертације
6. Копије диплома основних и мастер студија
7. Копије научних радова

С поштовањем,

Филип Крајинић

истраживач приправник

Filip Krajinić

ИНСТИТУТ ЗА ФИЗИКУ

ПРИМЉЕНО: 25. 07. 2024			
Рад.јед.	б р о ј	Арх.шифра	Прилог
0801	1335/2		

Научном већу Института за физику у Београду

Београд, 25.7.2024.

ПРЕДМЕТ: Мишљење руководиоца лабораторије о избору Филипа Крајинића у звање истраживач сарадник

Филипа Крајинић је запослен у Лабораторији за биофотонику, у оквиру Центра за фотонику. Израду докторске дисертације у области квантне холографије ради под руководством академика др Бранислава Јеленковића.

С обзиром да испуњава све предвиђене услове у складу са Законом о науци и истраживањима и Правилником о поступку, начину вредновања и квантитативном исказивању научноистраживачких резултата истраживача МПНТР, сагласна сам са покретањем поступка за избор Филипа Крајинића у звање истраживач сарадник.

За састав комисије за избор Филипа Крајинића у звање истраживач сарадник предлажем:

1. др Бранислав Јеленковић, научни саветник у пензији, Институт за физику Београд и дописни члан САНУ,
2. др Марија Ђурчић, научни сарадник, Институт за физику Београд
3. др Пеђа Михаиловић, редовни професор Електротехничког факултета Универзитета у Београду

Светлана Савић-Шевић

др Светлана Савић-Шевић

виши научни сарадник

Руководилац Лабораторије за биофотонику

Стручна биографија

Филип Крајинић је рођен 03.10.1997. године у Београду. Завршио је основну школу „Бора Станковић” у Београду као вуковац. Уписао је Четврту гимназију у Београду, коју је завршио са одличним успехом 2016. године. Исте године уписао је Електротехнички факултет Универзитета у Београду. Дипломирао је на одсеку за Физичку електронику, смер Наноелектроника, оптоелектроника и ласерска техника, 2020. године са просечном оценом 9,11. Дипломски рад, са називом „Холографско испитивање Фарадејевог ефекта”, је радио под менторством проф. др Пеђе Михаиловића и одбранио је у јулу 2020. године са оценом 10. Добитник је награде за најбољи дипломски рад на такмичењу ETF BAFA U.S.A. Мастер академске студије на Електротехничком факултету у Београду, на модулу за Наноелектронику и фотонику, уписао је у октобру 2020. године. Положио је све испите са просечном оценом 10. Мастер рад, са називом „Мерење поларизације светлости помоћу дигиталне холографије са симетричним референтним сноповима”, је радио под менторством проф. др Пеђе Михаиловића и одбранио је у септембру 2021. године са оценом 10. У октобру 2021. године уписао је докторске академске студије на Електротехничком факултету у Београду, на модулу за Наноелектронику и фотонику. Положио је све предвиђене испите по наставном плану докторских студија са просечном оценом 10. У јуну 2024. године успешно је одбранио свој припремни рад за пријаву теме докторске тезе са називом „Квантна холографија за осликавање објеката у средној инфрацрвеној области спектра без детекције интерагујућих фотона” (енгл. „*Quantum holography for object imaging in mid infrared spectrum with undetected photons*“) под менторством др Бранислав Јеленковић, научни саветник и дописни члан САНУ.

30. новембра 2021. године на седници Научног већа Института за физику стиче звање истраживач приправник. Од 2. децембра 2021. године је запослен у Институту за физику универзитета у Београду, при лабораторији за квантну биофотонику.

Током основних студија је био ангажован као студент демонстратор при извођењу лабораторијских вежби на предмету Практикум из конструисања електронских уређаја на одсеку за Физичку електронику.

У мају 2020. године је стекао сертификат *NI Certified LabVIEW Associate Developer* компаније *National Instruments* у трајању од две године.

Преглед научне активности

У досадашњем раду Филип Крајинић се бавио облашћу дигиталне холографије и њеном применом у сензорици и осликавању. Холографија, као област истраживања, користи технике интерферометрије како би снимио и репродуковао комплексну расподелу електричног поља оптичког таласног фронта. Предност холографије представља могућност да се поред расподеле интензитета оптичког таласа може репродуковати и расподела фазе оптичког таласа. Могућност репродукције и интензитета и фазе оптичког таласа омогућава пројектовање оптичког система који може да прочита било коју информацију уписану у расподелу амплитуде или фазе таласног фронта оптичког таласа.

Током основних студија Филип Крајинић је користио технике дигиталне холографије како би реализовао оптички сензорски систем за детекцију просторне расподеле екстерног магнетног поља. Применом Фарадејевог ефекта, кристал који испољава идукован магнето-оптички ефекат у присуству екстерног магнетног поља мења стање поларизације улазног ласерског снопа. Линеарно поларизована светлост се ротира за Фарадејев угао, који је линеарно сразмеран екстерном магнетном пољу. Поменута промена стања поларизације се може детектовати као промена расподеле интензитета оптичког таласа.

Касније током мастер студија, Филип Крајинић је модификовао холографски оптички систем тако да може да мери опште стање поларизације ласерске светлости. Упоредо мерење интензитета ортогоналних компоненти светлости и њиховом фазном разликом могуће је детектовати опште елиптично стање поларизације. Модификованим интерферометром који поседује три гране, могуће је једном аквизицијом слике доћи до стања поларизације.

Такође, Филип Крајинић учествује у истраживању љуспица крила лептира *Morpho didius* као сензора слике. Експериментално је показано да услед ласерске побуде која загрева љуспице на крилу индукује се благо померање љуспица које је линеарно пропорционално снаги побудног ласера. Техникама дигиталне холографије могуће је детектовати то благо померање мерењем фазе рефлектованог таласа о крило лептира. Будући да је крило апсорптивно у широком спектру зрачења, овакав биоинспиран детектор би могао да буде осетљив за ултравиолетно, видљиво и инфрацрвено зрачење.

Од почетка Хоризонт пројекта, започето је истраживање у области квантног осликавања. Употребом нелинеарних кристала могуће је добити парове спрегнутих фотона, који су корелирани по позицији, времену, импулсу и енергији. Услед тих особина могуће је направити такав интерферометар у коме један фотон из пара интерагује са узорком, док други фотон из пара поседује информацију о узорку и на њему може да се врши детекција. Ако би се изабрао такав нелинеаран кристал и задовољили одговарајући услови фазног упаривања, могуће је направити парове фотона дегенерисаних по таласној дужини, тако да један фотон буде у даљој инфрацрвеној области спектра и да други фотон буде у видљивој области спектра. Тада би се детекцијом фотона у видљивој области спектра могла детектовати информација коју је примио фотон у даљој инфрацрвеној области спектра који је интераговао са узорком без његове детекције.

Списак научних радова

Рад у врхунском међународном часопису (M21):

1. P. Atanasijevic, D. Grujic, **F. Krajinic**, P. Mihailovic, and D. Pantelic, "Characterization of a bioderived imaging sensor based on a Morpho butterfly's wing," *Opt. Laser Technol.*, vol. 159, p. 108919, Apr. 2023, doi: 10.1016/J.OPTLASTEC.2022.108919.

Рад у међународном часопису (M23):

1. **F. Krajinic**, P. Atanasijević, and P. Mihailović, "Object alignment in spatially multiplexed holograms applied to polarization sensing," *Rev. Sci. Instrum.*, vol. 95, no. 7, p. 73710, Jul. 2024, doi: 10.1063/5.0203429.

Саопштења са међународних скупова штамана у изводу (M34):

1. P. Atanasijevic, **F. Krajinic**, P. Mihailovic, and D. Pantelic, "Thermoelectric temperature control of Morpho butterfly wings used for radiation sensing," *16th Photonics Workshop*. 2023.
2. **F. Krajinic**, P. Atanasijevic, and P. Mihailovic, "Optical system for magnetic field spatial distribution measurement using digital holography," *17th Photonics Workshop*. 2024.

Регистрован патент на националном нивоу (M92):

1. П. Атанасијевић, **F. Krajinic**, and P. Mihailović, "Сензор за мерење магнетског поља одређивањем Фарадејевог ефекта помоћу дигиталне холографије," Завод за интелектуалну својину Републике Србије, Jan, 2024, [Online]. Available: <https://reg.zis.gov.rs/patreg/?t=p>.



УНИВЕРЗИТЕТ У БЕОГРАДУ
ЕЛЕКТРОТЕХНИЧКИ
ФАКУЛТЕТ

Д.Бр.2021/5006

Булевар краља Александра 73
П.Ф. 35-54, 11120 Београд, Србија
Тел: +381 11 3248464
Факс: +381 11 3248681

На основу члана 29. Закона о општем управном поступку („Сл. гласник РС”, бр.18/2016) и службене евиденције издаје се

УВЕРЕЊЕ

Крајинић (Ана) Филип, бр. индекса 2021/5006, рођен 03.10.1997. године, Београд, Звездара, Република Србија, уписан школске 2023/2024. године, у статусу: финансирање из буџета; тип студија: докторске академске студије; студијски програм: Електротехника и рачунарство, модул Наноелектроника и фотоника.

Према Статуту факултета студије трају (број година): три године.

Рок за завршетак студија: у двоструком трајању студија. Студенту се на лични захтев може продужити рок за завршетак студија до истека рока у троструком броју школских година за реализацију студијског програма.

Ово се уверење може употребити за регулисање војне обавезе, издавање визе, права на дечији додатак, породичне пензије, инвалидског додатка, добијања здравствене књижице, легитимације за повлашћену возњу, стипендије и у друге сврхе ради доказивања статуса студента.

Датум: 16.07.2024. године



Шеф Студентског одсека

Jelena Jevremović
Јелена Јевремовић



УНИВЕРЗИТЕТ У БЕОГРАДУ
ЕЛЕКТРОТЕХНИЧКИ
ФАКУЛТЕТ

Булевар краља Александра 73
П.Ф. 35-54, 11120 Београд, Србија
Тел: +381 11 3248464
Факс: +381 11 3248681

ТР: 840-0000001438666-48
ПИБ: 100206130
МБ: 07032498
ЈБКЈС: 02239

Број: 1275/25
Датум: 02-07-2024

На основу члана 40. Закона о високом образовању („Сл. гласник РС“, бр. 88/2017, 27/2018 - др. закон, 73/2018, 67/2019, 6/2020 - др. закон, 11/2021 - Аутентично тумачење, 67/2021, 67/2021 - др. закон и 76/2023), члана 112. Статута Универзитета у Београду („Гласник Универзитета у Београду“, бр. 201/2018, 207/2019, 213/2020, 214/2020, 217/2020, 230/2021, 232/2022, 233/2022, 236/22, 241/22, 244/23, 245/23, 247/23 и 251/23), члана 86. Статута Универзитета у Београду - Електротехничког факултета, члана 30. Правилника о докторским студијама на Универзитету у Београду („Гласник Универзитета у Београду“, бр. 191/2016, 212/2019, 215/2020, 217/2020, 228/21, 230/21 и 241/22), Наставно-научно веће на својој 899. седници одржаној 02.07.2024. године донело је

ОДЛУКУ о усвајању Извештаја Комисије о оцени научне заснованости теме докторске дисертације

Усваја се Извештај Комисије за оцену научне заснованости теме докторске дисертације под насловом „Квантна холографија за осликавање објекта у средњој инфрацрвеној области спектра без детекције интерагујућих фотона“, кандидата **Филипа Крајинића**, мастер инж. електротехнике и рачунарства.

Ментор докторске дисертације је др Бранислав Јеленковић, научни саветник и дописни члан САНУ.

Образложење

На основу Извештаја Комисије за оцену научне заснованости теме докторске дисертације, Наставно-научно веће Факултета је, у складу са својим овлашћењима, донело Одлуку као у диспозитиву.

Одлуку доставити надлежном Већу научних области Универзитета у Београду, ради давања сагласности на исту.

ДНА - Одлуку доставити Универзитету у Београду, ментору, Студентској служби и Архиви.

Припремила: Н. Прешћ



Председник Наставно-научног већа

Проф. др Дејан Гвоздић



Република Србија
Универзитет у Београду

Оснивач: Република Србија

Дозволу за рад број 612-00-02666/2010-04 од 12. октобра 2011.
године је издало Министарство просвете и науке Републике Србије

Електротехнички факултет, Београд

Оснивач: Република Србија

Дозволу за рад број 612-00-588/2008-04 од 17. новембра 2008.
године је издало Министарство просвете Републике Србије

УБ



Диплома

Филић, Ана, Крајинић

рођен 3. октобра 1997. године, Београд, Република Србија, уписан школске 2016/2017.

године, а дана 24. јула 2020. године завршио је основне академске студије, првог
степенa, на студијском програму Електротехника и рачунарство, обима 240
(двеста четрдесет) бодова ЕСПБ са просечном оценом 9,11 (девет и 11/100).

На основу тога издаје му се ова диплома о стиценом високом образовању и стручном називу
дипломирани инжењер електротехнике и рачунарства

Број: 11143400

У Београду, 29. октобра 2020. године

Декан
Проф. др Мило Томашевић

Ректор
Проф. др Иванка Појовић



Република Србија
Универзитет у Београду

Оснивач: Република Србија

Дозволу за рад број 612-00-02666/2010-04 од 12. октобра 2011.
године је издало Министарство просвете и науке Републике Србије

Електротехнички факултет, Београд

Оснивач: Република Србија

Дозволу за рад број 612-00-588/2008-04 од 17. новембра 2008.
године је издало Министарство просвете Републике Србије

УБ



Диплома

Филић, Ана, Крајинић

рођен 3. октобра 1997. године, Београд, Република Србија, уписан школске
2020/2021. године, а дана 28. септембра 2021. године завршио је мастер академске
студије, другог степена, на студијском програму Електротехника и рачунарство,
обима 60 (шездесет) бодова ЕСПБ са просечном оценом 10,00 (десет и 0/100).

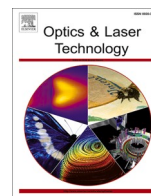
На основу тога издаје му се ова диплома о стеченом високом образовању и академском називу
мастер инжењер електротехнике и рачунарства

Број: 13281100

У Београду, 1. марта 2022. године

Декан
Проф. др Дејан Гвоздић

Ректор
Проф. др Владан Ђокић



Full length article

Characterization of a bioderived imaging sensor based on a Morpho butterfly's wing

Petar Atanasijevic^{a,*}, Dusan Grujic^b, Filip Krajinic^{a,b}, Pedja Mihailovic^a, Dejan Pantelic^b

^a University of Belgrade, School of Electrical Engineering, Bulevar kralja Aleksandra 73, 11120 Belgrade, Serbia

^b University of Belgrade, Institute of Physics Belgrade, Photonics Center, Pregevica 118, 11080 Zemun, Belgrade, Serbia



ARTICLE INFO

Keywords:
Biomimetics
Imaging sensor
Holography
Morpho butterfly

ABSTRACT

The interest in imaging sensors with broad spectral ranges has increased, driven by both the industry as well as the scientific community. Thus, the need to improve their performance and lower their market cost seems to be higher than ever. Nature provides an unexpected solution to this requirement, as the wing scales of a *Morpho* butterfly exhibit radiation induced displacement which can be measured using digital holography. The scales on a wing thus act as pixels on an area detector. However, no detailed characterization of the imaging performance of such a detector was reported. We address this issue and perform spatial and temporal characterization of a *Morpho* wing as an imaging sensor using digital holographic interferometry and thermal imaging. We believe that this is the first image acquisition using the wing of a butterfly, showing that the sensor has linear response at 405, 450, 660 and 980nm wavelengths, with sensitivity that depends linearly on the absorption of the specimen. The temporal response is demonstrated to be reproducible, with the 55ms time constant, while the spatial resolution of 1.46lp/mm at 20% contrast was achieved. The obtained results confirm the imaging capabilities of a *Morpho* wing and open the path toward novel bioinspired imaging techniques.

1. Introduction

As the field of biomimetics continuously develops, biological structures prove to be valuable in advancement of modern optical sensors [1], often relying on mechanisms of structural coloration in animals [2]. Among many biological materials used in sensing, the iridescent wings of a blue *Morpho* butterfly stand out because of their versatility. They were used to sense a range of quantities, from temperature [3], acoustic waves [4], pH [5], different gasses and solvents [6,7], to infrared (IR) radiation [8]–[10]. Already published review articles focus on fabrication of *Morpho* inspired sensing materials [11], different types of sensors [12,13], and sensing, security and energy applications [14]. Radiation detection attracts special attention as the need for low-cost imaging detectors with wide spectral ranges grows ever stronger.

The idea of IR radiation detection using the wings of a *Morpho* butterfly was first introduced in a paper by Pris *et al.* [8]. The authors measured the spectral reflectance change of the single-walled carbon nanotube (SWCNT) coated wing of a *Morpho sulkowski* butterfly in the visible spectrum. The spectral reflectance change was considered a consequence of thermal expansion in photonic multilayer structures on

the wing scales due to the incoming IR radiation. The same concept was implemented by Zhang *et al.* where instead of SWCNT, they coated the wing with gold, doubling the measured reflectance change [10]. A recent approach of IR detection demonstrated measurement of spectral reflectance change induced by IR stimulated desorption of vapor molecules from the nanostructures of the *Morpho* butterfly [15]. This approach showed superior sensitivity compared to other similar methods and was the first to allow for spectral selectivity in measurement.

Grujić *et al.* proposed a different approach in IR radiation detection using the wing of a *Morpho menelaus* [16] butterfly as a camera [9]. Displacement of wing scales was observed as a consequence of IR radiation. This movement was detected over the whole sample area using digital holographic interferometry. Holographic examination shows that total IR response of the sample at the irradiated point is due to the scale displacement.

We build upon the sensing mechanism outlined in [9] and examine the spatial, temporal, and spectral response of the *Morpho didius* wing [17]. Finally, we measure the radiation distribution using the *Morpho didius* wing, proving its imaging capabilities.

* Corresponding author.

E-mail address: petarat@etf.bg.ac.rs (P. Atanasijevic).

2. Materials and methods

The experimental results of this paper are obtained using the *Morpho didius* species of the *Morpho* butterfly genus. The similar effect of wing scale movement due to radiation was observed previously in *M. menelaus* butterfly [9]. Other types of *Morphos* exhibiting similar optomechanical properties [18] are therefore candidates for image sensing as well. The spatial and temporal response (*i.e.* the movement of wing scales) of the sample's iridescent side to incoming radiation was investigated using digital holography.

2.1. Insect specimens and sample preparation

A selected part of the wing of a *M. didius* butterfly was cut and mounted on an aluminum plate, with the non-iridescent side facing the aluminum. The butterfly's wing was not modified in any of the presented experiments. The wing itself is fragile and can easily be damaged during mechanical cutting. To overcome this issue, the samples were cut using a commercial CO_2 laser cutter without a protective air stream. The wing was cut to avoid veins which are stiffer than the membrane, and almost completely non-responsive due to a limited number of scales covering them.

During the experiments described in this paper beeswax was used to fix the sample to a plastic strip. The strip was then mounted to the aluminum plate holder using double adhesive tape. The photograph of the prepared sample is shown in Fig. 1. The wax filled the sample's backside, providing a uniform attachment, but increasing the sensor response time. Improving the response time was attempted by changing the properties of the adhesive material, and by the removal of the plastic strip and the adhesive tape. The second sample had the thickness of the beeswax decreased. The third one used wax with TiO_2 . The fourth sample used a heat sink pad ($240W/mK$), and the fifth used a saturated sugar solution instead of wax.

2.2. Setup for wing excitation and measurement

The holographic part of the setup is a modified version of the *Single-beam dual-view* setup [9,19]. Cameras used for hologram recording were Nikon 1 V3 digital camera (5232×3488 resolution, 60fps) and Basler acA2440-75um (2448×2048 resolution, 75 fps). Coherent Verdi V5 DPSS laser with a wavelength of $532nm$ was used for holography. Its irradiance was set to $35\mu W/mm^2$, to prevent significant heating by the measurement. Apart from the apparatus for holographic measurements, the setup incorporates a thermal camera FLIR A65 with 30 Hz frame rate, as well as the excitation section (ES) that was interchanged to suit the experimental requirements. Fig. 2 a) shows the main experimental setup with different ES shown in Fig. 2 b). The excitation beam (EB) induced temperature change ΔT and consequently, displacement ΔX of wing scales is illustrated in Fig. 2 c). The displacement was detected by computing the difference between phase images reconstructed from a

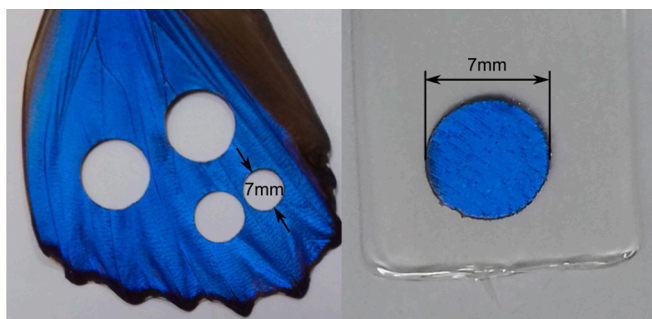


Fig. 1. Image of a circular sample cut from the *M. didius* wing and placed on a plastic strip covered with wax.

series of recorded holograms.

Excitation section one (ES1) was used for wing calibration, spectral and temporal response characterization using four laser diodes (LD) three in the visible ($405, 450$ and $660nm$), and one in the near-infrared (NIR) part of the spectrum ($980nm$). LDs were controlled and synchronized with the rest of the system by the microcontroller. The neutral density filter (NDF) was used to adjust the EB power from $600\mu W$ to $20mW$. Beam splitter (BS) was inserted into the EB path to provide a monitoring signal for a photodiode power meter (PD300 Ophir photonics).

In another configuration (ES2) a He-Ne laser with a wavelength of $632.8nm$ and a known Gaussian beam profile was used to perform a "one-shot" spatial characterization. The lens was used to expand the Gaussian beam over the sample area, to characterize differences in wing scales ("pixels").

ES3 was used to resize and reshape the EB, so an image could be projected onto the sample. Images were defined by the beam mask. A version of the Slanted Edge Method [20,21] was used to estimate the effective resolution of the imaging system. The edge spread function (ESF) was recorded using the wing as an area detector. From the ESF, the line spread function (LSF) was derived, and the modulation transfer function (MTF) was calculated [22].

2.3. Acquisition software and digital hologram reconstruction methods

The synchronization of the thermal camera, with the digital camera and the exciting lasers, was performed using an application developed in LabVIEW. The thermal images were non-uniformity corrected before every acquisition.

Hologram reconstruction was performed using the shifted and scaled Fresnel reconstruction method [24], with the scaling operation performed in the destination plane instead of the source plane. A set of equations for hologram reconstruction and displacement calculation is presented in Appendix A. The phase difference images were median filtered to reduce the influence of noise. Phase unwrapping was conducted in the time domain. Phase differences on a pixel level were calculated between successive holograms during the recording, and the total induced phase difference was calculated as a sum of the calculated increments.

2.4. Experiment design and data processing

2.4.1. Calibration function, spectral characterization and temporal response

To determine the wing's calibration function, spectral properties and temporal response, the ES1 setup was used. LDs with wavelengths of $405, 450, 660$, and $980nm$ were used to excite the wing sample for $200ms$. LD beams were of different irradiance distributions and sizes. The induced phase difference holographic images, as well as thermal images, were analyzed to correlate the phase difference after $200ms$ exposure, with the EB irradiance and the induced temperature change. For the calibration function, we calculate the mean value of the induced phase change and establish its relationship to the average EB irradiance according to Equation (1).

$$\varphi_{avg} = K_{\lambda} \cdot I_{avg} \quad (1)$$

I_{avg} represents the average EB irradiance calculated by dividing the EB power by its spot size, and K_{λ} is a proportionality constant denoting the measurement sensitivity at a specified wavelength. Further discussion on the choice of Equation (1) in context of the reconstruction algorithm is presented in Appendix A.

Temporal behavior was analyzed by recording a series of successive holograms, and normalizing the response.

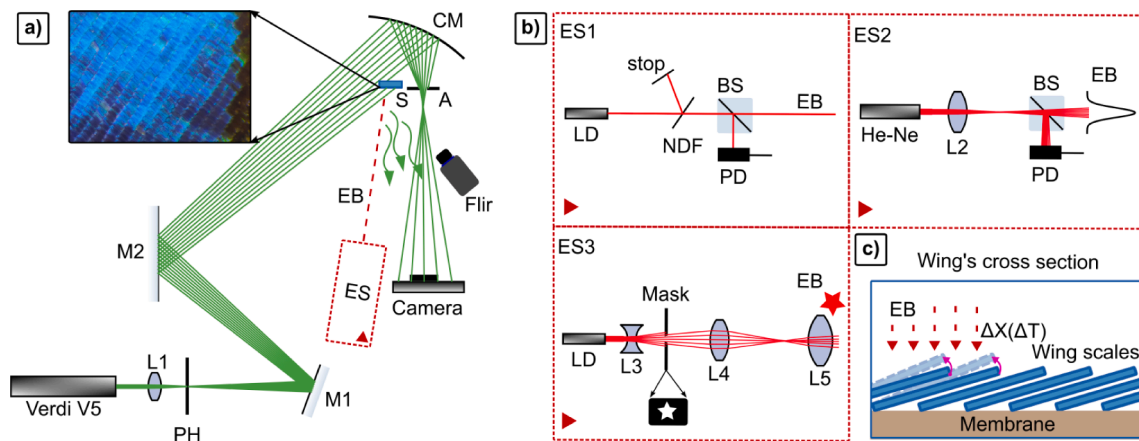


Fig. 2. a) Modified Single-beam dual-view digital holographic setup. b) Interchangeable Excitation Sections. c) The illustration of the effect of the radiation-induced temperature change (ΔT), and displacement (ΔX). L1, L2, L3, L4, L5 – Lenses, M1, M2 – Plane Mirrors, CM – Concave Mirror, EB – Excitation Beam, PH – Pinhole, S – Sample, A – Aperture, LD – Laser Diode, PD – Photodiode, NDF – Neutral Density Filter, BS – Beam Splitter. Light beams are drawn using the Ray Optics extension in Inkscape [23].

2.4.2. Spatial response

The spatial response of the wing was characterized by the ES2. He-Ne laser with a wavelength of 632.8nm was chosen because its wavelength is close to the 660nm wavelength where the sample was calibrated, while it has a well-defined beam profile.

To examine the imaging capabilities of the *M. didius* wing, we used the ES3 setup with five different beam masks: concentric circles, bright and dark line pairs, a letter X, a star, and a straight edge illumination used for the Slanted Edge Method. The phase difference response to the straight edge was used to calculate the ESF. The calculation involved the averaging of 50 rows along the edge. The averaged line was further filtered before the numerical differentiation to obtain the LSF. The LSF was Fourier transformed to generate the MTF.

3. Results

Examples of the reconstructed hologram intensity image, pseudo colored phase difference image and thermal image are presented in Fig. 3.

3.1. Calibration function and spectral characterization

The results for different EB wavelengths are shown in Fig. 4 a). Experimental results confirm the assumed linear relationship between the mean phase change and the average irradiance. The sample exhibits high sensitivity in the red region of the visible spectrum and near the ultraviolet (UV) region of the spectrum. The sensitivity drops both near the blue wavelengths and in the NIR range.

The relation between the induced mean phase change and the induced mean temperature change is shown in Fig. 4 b). The mean temperature change is calculated from thermal images using the same principle applied to phase change calculations. The relationship between phase change and temperature is independent of the wavelength of the EB. The displacement of wing scales is thus a consequence of temperature change caused by the incoming radiation. Therefore, only one straight line was fitted through all measured points, regardless of wavelength. The slope of the fitted line is 9.971rad/K , which corresponds to a displacement of $0.478\mu\text{m/K}$ (equations presented in Appendix A).

The results from Fig. 4 a) and b) suggest that the overall sensitivity of the proposed sensor is determined by the spectral absorption of the wing. To prove this hypothesis, the spectral reflectance and transmittance of a *M. didius* wing sample were measured, and the absorption was calculated in the $390 - 1000\text{nm}$ range. The reflectance measurements were performed using an RSA-FO-150 integrating sphere, and the transmittance measurements were conducted in a transmission geometry. Percentages of light transmitted and reflected by this intact wing sample are plotted with solid lines in Fig. 4 c). The results are similar to the spectra found in literature [25]. The absorption spectrum is plotted with a solid line in Fig. 4 d), together with the measured sensitivity K_λ obtained from the wing calibration. The high sensor sensitivity wavelengths correspond to high absorption spectral regions. While the sensitivity in the blue-green region drops because of high interferometric wing reflection [25], the sensitivity drop in the NIR range is due to both the increase in reflectance and transmittance of the sample. From the plot in Fig. 4 d) the relation between absorption and sensitivity

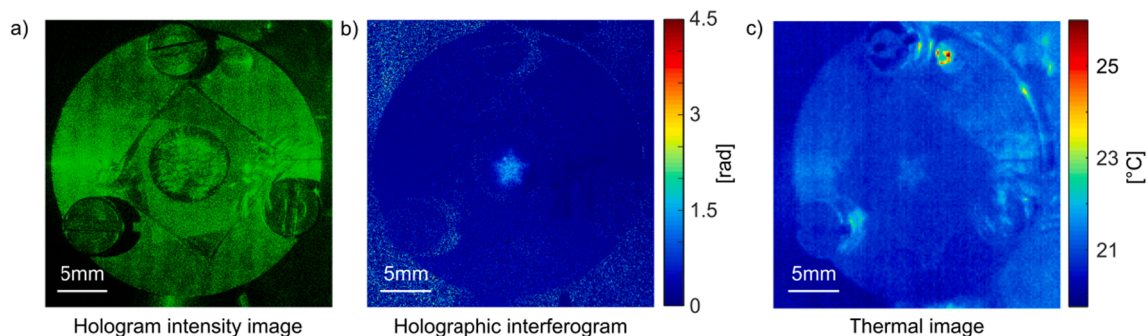


Fig. 3. a) A part of the intensity image of a reconstructed hologram, showing a sample fixed on an aluminum mount. b) The same part of the phase difference image of two holograms, showing a star-shaped area where the 660nm , 3.9mW laser radiation was present for 200ms . c) Thermal image showing the radiation-induced temperature change (different measurement with the rotated star).

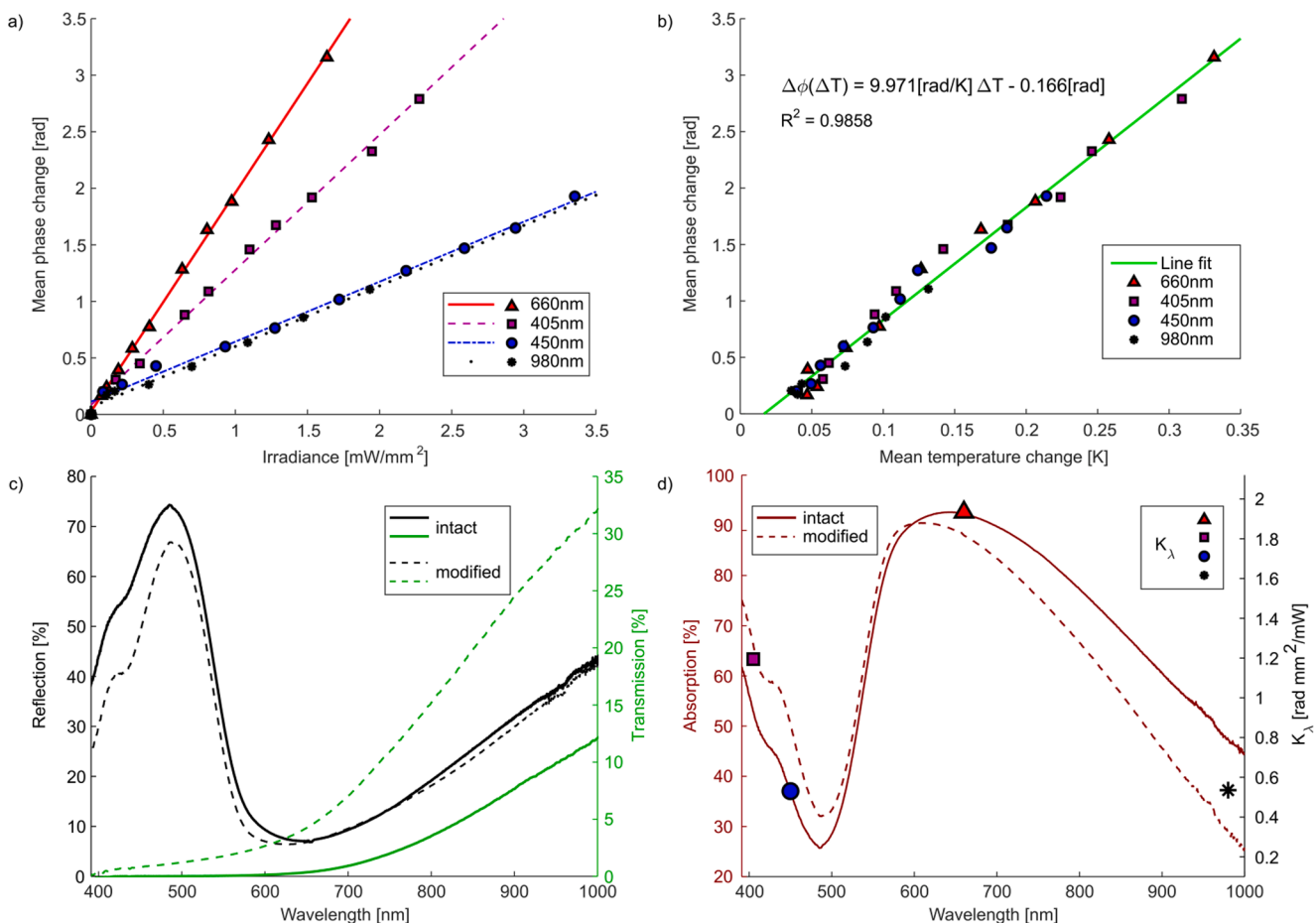


Fig. 4. a) Relation (calibration function) between the mean phase change and mean beam irradiance after 200 ms of exposure, for four different wavelengths. b) Relation between the mean phase change and the mean induced temperature change after 200 ms exposure, for four different wavelengths. c) Spectral dependence of reflectance (left axis, black) and transmittance (right axis, green) for the intact wing (solid line), and for the wing modified by the removal of the scales on the underside of the membrane (dashed line). d) Spectral dependence of sensitivity K_λ (right), and absorption for the intact *M. didius* wing (left, solid line), and the wing modified by the removal of the scales on the underside of the membrane (left, dashed line). (For interpretation of the references to colour in this figure legend, the reader is referred to the web version of this article.)

is confirmed.

To further determine the contribution of different types of scales in the spectral properties of absorption, the scales on the underside of the membrane were removed mechanically, and the reflectance and transmittance measurements were repeated for this wing sample. Percentages of light transmitted, reflected, and absorbed by the modified wing sample are plotted with the dashed lines in Fig. 4 c) and d) respectively. The removal of the underside scales increased the transmittance, while the reflectance was not influenced significantly. Thus, it can be concluded that the underside scales contribute to the absorption and the temperature change of the sample, especially in the NIR region.

The results confirm a linear sensor response, while the spectral properties are governed by absorption. This gives rise to the idea that the absorption could be artificially enhanced by deposition of absorbing materials on the wing's surface, as previously reported in the literature [8], thus increasing the sensitivity in a desired part of the spectrum. The response to the UV region of the spectrum should be high even in a non-modified wing, due to the presence of melanin.

3.2. Temporal response

The average of 10 normalized temporal responses to different (200ms, 660nm) EB powers, with the corresponding standard deviation calculated and shown for every point is presented in Fig. 5 a).

Due to a very small standard deviation at every point, one may

conclude that the phase response is highly reproducible. The shape of the obtained curve during the heating (Laser on) and cooling (Laser off) periods suggests a first order system response, following the laws of heating and cooling governed by Equations (2) and (3) respectively:

$$T(t) = T_A + P\theta_e \left[1 - \exp\left(-\frac{t}{\tau}\right) \right], \tau = mc\theta_e \tag{2}$$

$$T(t) = T_A + (T_{max} - T_A) \exp\left(-\frac{t}{\tau}\right), \tag{3}$$

where T and T_A denote current wing temperature and ambient temperature respectively, P represents the EB power, τ is the time constant, m and c represent the mass and specific heat determined by the butterfly's wing, while t stands for time. θ_e is the equivalent thermal resistance between the sample and the ambient. It incorporates both the heat conduction through the wax, adhesive tape, and the aluminum mount, as well as convection due to exposure to the surrounding air. The phase change will follow the same time dependence as temperature change considering the linear relationship determined in the previous subsection. Derivation of the Equations (2) and (3) is provided in Appendix B.

The step response of the samples was examined for both laser heating and cooling. The first sample with the thick layer of beeswax showed a time constant of 352ms. A large value of the time constant is a consequence of choosing the beeswax on a plastic strip as an adhesive layer-

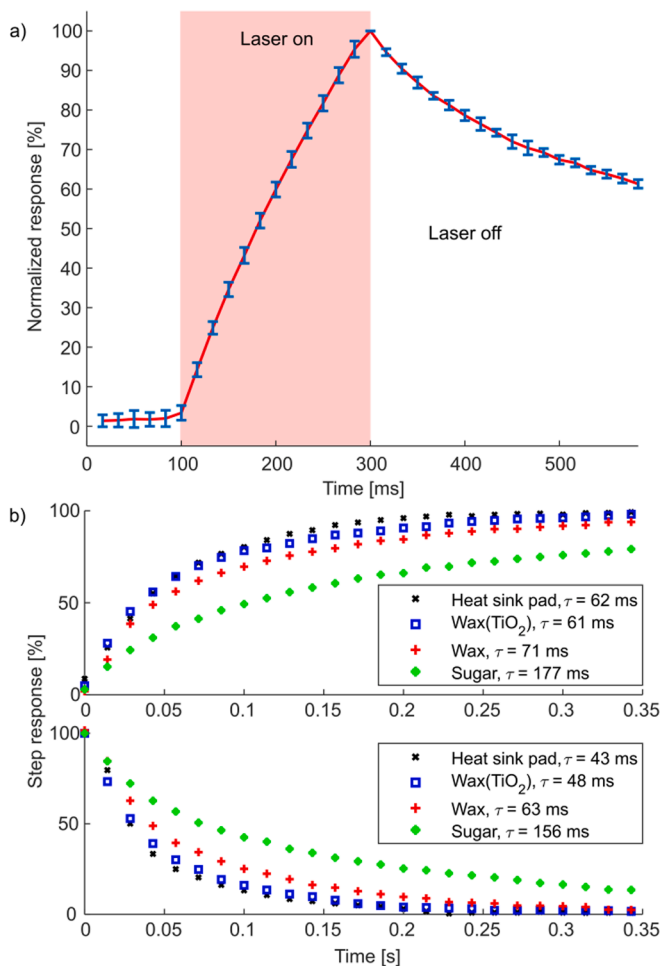


Fig. 5. a) Average normalized phase change in time for ten 660 nm measurements with different EB power. b) Normalized phase step response to heating (upper plot) and cooling (lower plot), with respective time constants.

rial. Even though it provides good mechanical support for the fragile wing sample, a thick layer of wax is a poor heat conductor. This limits the temporal response of this version of the proposed sensor.

The normalized phase change step response of a point on a butterfly’s wing for improved samples (two to five) is presented in Fig. 5 b). A time constant decrease by a factor of two to six is apparent compared to the original sample. Even though the heat sink pad shows the smallest average time constant of only 53 ms, the adhesion of the wing to the pad was not optimal. Thus, the thin layer of wax with TiO_2 emerges as the optimal solution with the average time constant of 55 ms and proper wing to mount adhesion.

As the Equations (2) and (3) suggest, the decrease in time constant also decreased the average temperature change proportionally, thus decreasing the sensor sensitivity forcing the compromise between sensitivity and response rate.

3.3. Spatial response

The image in Fig. 6 a) is a photograph of the expanded Gaussian beam, taken using the digital camera. When fitted to a two-dimensional Gaussian distribution function, it showed the total beam width of 6.96 mm and 7.06 mm in the horizontal and vertical directions respectively. The term “total width” refers to a width of $1.5w(z)$ which contains 99% of the total beam power. $w(z)$ is the beam radius at a distance z from the waist, where the observation occurs [26].

Fig. 6 b) shows the induced holographic phase difference image of the wing after the 617 ms exposure to the expanded Gaussian beam. The fit of the two-dimensional Gaussian distribution to the obtained phase difference image resulted in an R^2 value of 0.9755, proving the ability to measure radiation distribution using the wing of a butterfly. The total width of the fitted distribution was 7.48 mm and 8.55 mm in the horizontal and vertical directions respectively. Overestimation of the beam width is a consequence of a sensing mechanism that involves heat transport and displacement not only in the plane perpendicular to the sample but in the lateral plane as well. The difference in horizontal and vertical beam widths is a consequence of the fact that wing scales are inherently asymmetrical with their length two times larger than their width.

Fig. 6 c), e) and g) show a photograph of a sample, illuminated by 660 nm LD radiation with three of the aforementioned five masks. The

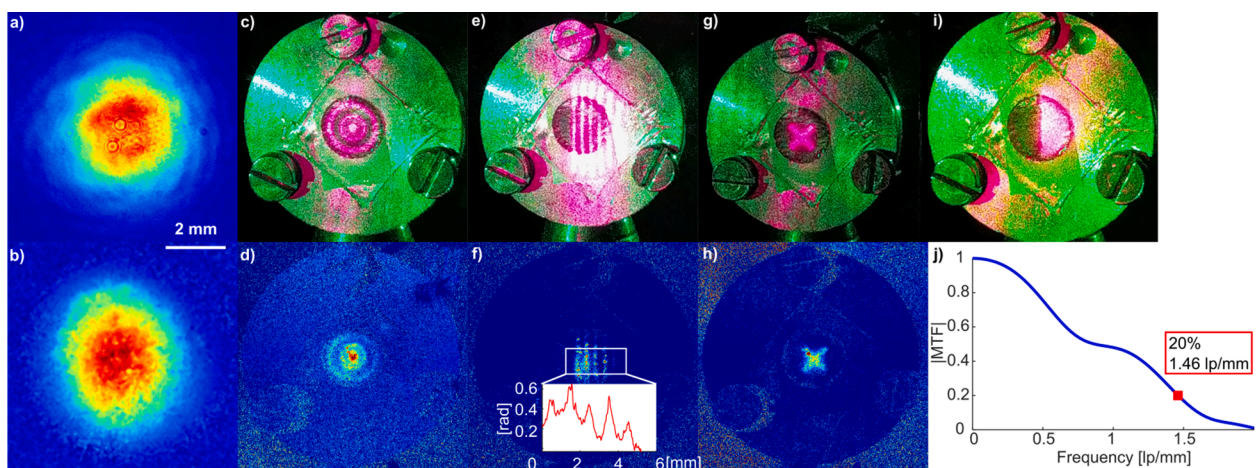


Fig. 6. Demonstration of the spatial response properties of a *M. didius* wing as an imaging sensor. a) The photograph of a Gaussian beam profile recorded by a CMOS camera. b) Phase difference induced by the same Gaussian beam, imaged holographically on the wing. c) Photograph of the sample illuminated by 660 nm laser radiation shaped like a group of concentric circles. d) Phase difference induced by the concentric circles, imaged holographically on the wing. e) Photograph of the sample illuminated by 660 nm laser radiation shaped like a group of line pairs with a frequency of 1 lp/mm. f) Phase difference induced by the line pairs, imaged holographically on the wing. g) Photograph of the sample illuminated by 660 nm laser radiation shaped like an X sign. h) Phase difference induced by the X sign, imaged holographically on the wing. i) Photograph of the sample illuminated by 660 nm laser radiation shaped to form an edge. j) MTF calculated using the Slanted Edge Method.

spatial frequency of the line pairs in Fig. 6 e) is $1lp/mm$. Fig. 6 d), f) and h), show the phase difference images measured as a response to the radiation distributions of Fig. 6 c), e) and g) respectively. Fig. 3 b) also shows the phase difference image, where a shape of a small star can be observed as a result of the fourth beam mask which was star-shaped. To the best of our knowledge, these phase maps are the first images of light intensity distribution measured using a wing of a butterfly as an imaging sensor.

The inset in Fig. 6 f) shows a line that was generated by averaging 70 successive rows in the exposed region of the phase difference image. The line is a profile of phase change that shows peaks and dips corresponding to the light and dark regions of the illumination distribution. Knowing the pixel spacing in the hologram reconstruction plane, it was possible to generate the length axis in the plot. From this phase profile, a line pair frequency was calculated to be $1lp/mm$ which is consistent with the actual line pair frequency measured beforehand. Time evolution of the wing's phase response to the line pairs and the Gaussian beam is presented in a video sequence in Appendix C.

Finally, the Slanted Edge Method and its results are presented in Fig. 6 i) and j). Fig. 6 i) shows the photograph of the sample illuminated by a straight edge. The obtained MTF is shown in Fig. 6 j). Using this plotted dependence, we estimated (in units of spatial frequency) the resolving capabilities of the proposed sensing mechanism. It is estimated that the illumination with a spatial frequency of $1.46lp/mm$ will cause the amplitude of the MTF to drop to 20%. This estimate agrees with the results observed in other phase images shown in Fig. 6.

The reflection of light from the Morpho butterfly's wing is angle dependent, as discussed previously [27]. The response to the EB is expected to follow the angular dependence of absorption. In our measurements, the angle of the EB was fixed.

4. Discussion

To compare the performance of the proposed sensing mechanism with the conventional imaging detectors, the presented results are converted to standardized quantities. One of the fundamental quantities of a camera is its pixel size which limits its spatial resolving capabilities. For a *M. didius* wing, the pixel is one wing scale with a size of $100 \times 200\mu m$ [18]. The wing scales are overlapping decreasing effective pixel size and causing crosstalk between neighboring scales. The standard deviation of the phase noise of a non-excited sample was measured to be $0.046rad$, and the maximum measured signal was $15.16rad$. Thus, the dynamic range of the sensor is calculated to be $50dB$, which is slightly less compared to conventional detectors, *i.e.*, CCD. Treating the sensor as a first order system with an average time constant of $55ms$ (wax with TiO_2 adhesive), $-3dB$ cut off frequency is calculated to be $5Hz$, while the attenuation of $10dB$ corresponds to a frequency of $29Hz$, close to a $30Hz$ frame rate of standard cameras. Based on the presented values, the currently investigated biological sample is inferior to the state of the art CCD/CMOS, short-wave infrared, and thermal detectors in their individual spectral ranges. However, contrary to detectors possessing an energy bandgap, the excess energy of the lower wavelength photons absorbed by a wing scale is not wasted but contributes to temperature increase. Unlike the CCD, the wing's spectral sensitivity to the number of photons is proportionate to the photon energy increasing the response in the UV where the absorption is already high. Furthermore, the sensing mechanism based on absorption and heating is applicable across the spectrum and enables for the uncooled detection over a broad spectral range. Such a broad spectral range imaging sensor can find use in security and surveillance, as well as in scientific and industrial applications.

5. Conclusions

We demonstrated the imaging capabilities of *Morpho* butterfly wing scales interrogated by digital holography. Calibration of the proposed sensor in the visible and NIR parts of the spectrum resulted in a highly linear response function. The sensitivity of this function was shown to be wavelength dependent and to follow the absorption curve of the *M. didius* sample throughout the visible spectrum. Based on this result we claim that the sensitivity of the proposed imaging sensor can be artificially modified by deposition of absorbing materials on the wing scales, as previously demonstrated in the literature. Using our holographic setup, we obtained a very high sensitivity to the induced temperature change with a value of $9.971rad/K$. Temporal response of the wing was shown to be highly reproducible, while response rate depends on the material used to mount the sample to the holder. Finally, we demonstrated image acquisition using the butterfly's wing with the resolving ability of $1.46lp/mm$ for the MTF value of 20%. Not much research was published regarding bioderived imaging sensors. Our findings open at least two paths in the field. One is sample functionalization through chemical and/or physical pixel modification to enhance the response in different spectral regions. The other is implementing the proposed sensing principle in artificial porose materials.

CRedit authorship contribution statement

Petar Atanasijevic: Conceptualization, Methodology, Software, Data curation, Investigation, Visualization, Writing – original draft, Writing – review & editing. **Dusan Grujic:** Methodology, Data curation. **Filip Krajinic:** Data curation. **Pedja Mihailovic:** Conceptualization, Methodology, Resources, Supervision, Formal analysis, Funding acquisition, Investigation, Writing – original draft, Writing – review & editing. **Dejan Pantelic:** Conceptualization, Methodology, Resources, Supervision, Funding acquisition, Formal analysis, Investigation, Project administration, Writing – original draft, Writing – review & editing.

Declaration of Competing Interest

The authors declare that they have no known competing financial interests or personal relationships that could have appeared to influence the work reported in this paper.

Data availability

Data will be made available on request.

Acknowledgments

The authors acknowledge funding provided by the Institute of Physics Belgrade through the grants by the Ministry of Education, Science and Technological Development of the Republic of Serbia. This work was also supported by the NATO, Science for Peace and Security Project SPS G5618.

The authors would like to thank Dr. Željko Janićijević from the Institute of Radiopharmaceutical Cancer Research, Helmholtz-Zentrum Dresden-Rossendorf for his valuable comments and suggestions regarding the preparation of the manuscript, and SistemCD for their help and patience in cutting the fragile butterfly wings using their CO_2 lasers.

The authors would like to thank Dr. Miloš Tomić, Dr. Lidija Mančić, Dr. Ivana Dinić and Dr. Marina Vuković from the Institute of Technical Sciences of the Serbian Academy of Sciences and Arts, Belgrade, Serbia for their help and expertise in performing the wing's reflectance measurements.

Appendix A. . Shifted and scaled Fresnel hologram reconstruction, and displacement calculation

The Fresnel diffraction calculation for hologram reconstruction can be expressed in the convolution form using the following equation [24]:

$$u_2(x_2, y_2) = \frac{e^{ikz}}{i\lambda z} \iint u_1(x_1, y_1) e^{\frac{i\pi}{\lambda z} [(x_2-x_1)^2 + (y_2-y_1)^2]} dx_1 dy_1 \quad (A.1)$$

where u_i is the complex wave field, λ is the laser wavelength, and indices 1 and 2 denote the hologram plane and the object plane separated by the distance z . The coordinates in the object plane (x_2, y_2) should be scaled by a factor of s , and shifted by a_x and a_y in the x and y directions respectively, giving new equations:

$$\begin{aligned} (sx_2 - x_1 + a_x)^2 &= s(x_2 - x_1)^2 + x_2^2(s^2 - s) + x_1^2(1 - s) + a_x^2 + 2sx_2a_x - 2x_1a_x \\ (sy_2 - y_1 + a_y)^2 &= s(y_2 - y_1)^2 + y_2^2(s^2 - s) + y_1^2(1 - s) + a_y^2 + 2sy_2a_y - 2y_1a_y \end{aligned} \quad (A.2)$$

for the quadratic terms in the exponent of the Fresnel diffraction equation. The expression can be calculated as a convolution using the Fourier transform:

$$u_2(x_2, y_2) = C_z \mathcal{F}^{-1} \{ \mathcal{F} \{ u_1(x_1, y_1) \bullet e^{i\phi_u} \} \mathcal{F} \{ e^{i\phi_h} \} \} \quad (A.3)$$

in which the terms C_z , $e^{i\phi_u}$ and $e^{i\phi_h}$ represent:

$$\begin{aligned} C_z &= \frac{e^{ikz}}{i\lambda z} e^{\frac{i\pi}{\lambda z} ((s^2-s)(x_2^2+y_2^2) + a_x^2+a_y^2 + 2s(x_2a_x+y_2a_y))} \\ e^{i\phi_u} &= e^{\frac{i\pi}{\lambda z} ((1-s)(x_1^2+y_1^2) - 2(x_1a_x+y_1a_y))} \\ e^{i\phi_h} &= e^{\frac{i\pi}{\lambda z} s(x_1^2+y_1^2)}. \end{aligned} \quad (A.4)$$

The resolution of the reconstructed phase images depends on the scaling factor s of the Shifted-Fresnel reconstruction algorithm. This means that by changing the scaling factor during reconstruction, the number of points inside the illuminated area is effectively changed. Since the measurement result must be independent of s , the metric introduced in Equation (1) is appropriate because the mean phase change in the illuminated area, calculated as:

$$\varphi_{avg} = \frac{1}{N} \sum_{i=1}^N \Delta\varphi_i \quad (A.5)$$

stays the same. In the previous equation N denotes the number of points with the observed phase change, while $\Delta\varphi_i$ is the value of the phase change of every point. For a point to be added to this sum, it must be in a determined region of interest, and it must have $\Delta\varphi_i$ larger than a threshold phase change determined by an average of the background. Sometimes, even after median filtering of the obtained phase differences, the effects of noise can still be apparent. However, because of the averaging nature of the φ_{avg} , the noise effects are further reduced, yielding more reliable results.

After the reconstruction and the hologram phase difference $\Delta\varphi$ calculation, the displacement of the wing scales is calculated using the following expression [28]:

$$\Delta\varphi = \vec{d} \cdot \vec{e} = \frac{2\pi}{\lambda} d(1 + \cos\theta) \quad (A.6)$$

where \vec{d} is the displacement vector, \vec{e} is the sensitivity vector and θ is the angle between the beam illuminating the object, and the beam reflected from the object toward the hologram recording plane. In the previous expression, the wing scale displacement vector is assumed to be approximately perpendicular to the sample surface. In the holographic setup shown in Fig. 2 a) the angle θ is equal to 40° , resulting in a final expression for the wing scale displacement:

$$d = 0.283 \frac{\Delta\varphi\lambda}{\pi}. \quad (A.7)$$

Appendix B. . Radiation induced temperature change time dependence

The heat transfer of the wing during the laser heating is governed by the equation:

$$mcdT = Pdt - \frac{T - T_A}{\theta_E} dt. \quad (B.1)$$

By integrating (B.1), the time dependence of wing temperature during the laser heating is obtained as:

$$T = P\theta_E \left[1 - \exp\left(-\frac{t}{mc\theta_E}\right) \right] + T_A. \quad (B.2)$$

When the laser is turned off, only the heat loss remains on the right-hand side:

$$mcdT = -\frac{T - T_A}{\theta_E} dt. \quad (B.3)$$

Integrating the previous equation results in the time dependence of the wing temperature during cooling:

$$T = (T_{max} - T_A) \exp\left(-\frac{t}{mc\theta_E}\right) + T_A. \quad (\text{B.4})$$

Appendix C. . Time evolution of the wing's phase response to the line pair and the Gaussian beam shaped illumination

Supplementary material





Supplementary data to this article can be found online at <https://doi.org/10.1016/j.optlastec.2022.108919>.

References

- [1] R.J. Martín-Palma, M. Kolle, [INVITED] Biomimetic photonic structures for optical sensing, *Opt. Laser Technol.* 109 (2019) 270–277, <https://doi.org/10.1016/j.optlastec.2018.07.079>.
- [2] A.R. Parker, N. Martini, Structural colour in animals—simple to complex optics, *Opt. Laser Technol.* 38 (4) (2006) 315–322, <https://doi.org/10.1016/j.optlastec.2005.06.037>.
- [3] T. Lu, S. Zhu, J. Ma, J. Lin, W. Wang, H. Pan, F. Tian, W. Zhang, D.i. Zhang, Bioinspired thermo-responsive photonic polymers with hierarchical structures and their unique properties, *Macromol. Rapid Commun.* 36 (19) (2015) 1722–1728.
- [4] L. Zhou, J. He, W. Li, P. He, Q. Ye, B. Fu, P. Tao, C. Song, J. Wu, T. Deng, W. Shang, Butterfly Wing Hears Sound: Acoustic Detection Using Biophotonic Nanostructure, *Nano Lett.* 19 (4) (2019) 2627–2633.
- [5] Q. Yang, S. Zhu, W. Peng, C. Yin, W. Wang, J. Gu, W. Zhang, J. Ma, T. Deng, C. Feng, D.i. Zhang, Bioinspired fabrication of hierarchically structured, pH-tunable photonic crystals with unique transition, *ACS Nano* 7 (6) (2013) 4911–4918.
- [6] J. He, N.S. Villa, Z. Luo, S. An, Q. Shen, P. Tao, C. Song, J. Wu, T. Deng, W. Shang, Integrating plasmonic nanostructures with natural photonic architectures in Pd-modified: Morpho butterfly wings for sensitive hydrogen gas sensing, *RSC Adv.* 8 (57) (2018) 32395–32400.
- [7] R. Ahmed, X. Ji, R.H. Atta, A.A. Rifat, H. Butt, Morpho butterfly-inspired optical diffraction, diffusion, and bio-chemical sensing, *RSC Adv.* 8 (48) (2018) 27111–27118.
- [8] A.D. Pris, Y. Utturkar, C. Surman, W.G. Morris, A. Vert, S. Zalyubovskiy, T. Deng, H.T. Ghiradella, R.A. Potyrailo, Towards high-speed imaging of infrared photons with bio-inspired nanoarchitectures, *Nat. Photonics* 6 (3) (2012) 195–200.
- [9] D. Grujić, D. Vasiljević, D. Pantelić, L. Tomić, Z. Stamenković, B. Jelenković, Infrared camera on a butterfly's wing, *Opt. Express* 26 (11) (2018) 14143.
- [10] F. Zhang, Q. Shen, X. Shi, S. Li, W. Wang, Z. Luo, G. He, P. Zhang, P. Tao, C. Song, W. Zhang, D.i. Zhang, T. Deng, W. Shang, Infrared detection based on localized modification of Morpho butterfly wings, *Adv. Mater.* 27 (6) (2015) 1077–1082.
- [11] Y. Zhu, W. Zhang, D.i. Zhang, Fabrication of Sensor Materials Inspired by Butterfly Wings, *Advanced Materials Technologies.* 2 (7) (2017) 1600209.
- [12] Q. Li, Q. Zeng, L. Shi, X. Zhang, K.-Q. Zhang, Bio-inspired sensors based on photonic structures of Morpho butterfly wings: a review, *J. Mater. Chem. C* 4 (9) (2016) 1752–1763, <https://doi.org/10.1039/C5TC04029A>.
- [13] H. Xue, D. Liu, D. Chi, C. Xu, S. Niu, Z. Han, L. Ren, Toward the Burgeoning Optical Sensors with Ultra-Precision Hierarchical Structures Inspired by Butterflies, *Adv. Mater. Interfaces* 8 (15) (2021) 2100142.
- [14] M.I. Osotsi, W. Zhang, I. Zada, J. Gu, Q. Liu, D. Zhang, Butterfly wing architectures inspire sensor and energy applications, *Natl. Sci. Rev.* 8 (3) (Mar. 2021), <https://doi.org/10.1093/nsr/nwaa107>.
- [15] Q. Shen, S. Ma, Z. Luo, S. An, J. He, R. Zhang, P. Tao, C. Song, J. Wu, R. A. Potyrailo, T. Deng, W. Shang, Butterfly Wing Inspired High Performance Infrared Detection with Spectral Selectivity, *Adv. Opt. Mater.* 8 (6) (2020) 1901647.
- [16] C. von Linnaeus and others, "Systema naturae, vol. 1," *Systema naturae, Vol. 1*, 1758.
- [17] C. Hopffer, *Neue Lepidopteren von Peru und Bolivia*. 1874.
- [18] S. Berthier, G. Kattawar, Iridescences: The physical colors of insects, *Opt. Eng.* (2008), <https://doi.org/10.1063/1.2883914>.
- [19] D.V. Pantelic, D.Z. Grujic, D.M. Vasiljevic, Single-beam, dual-view digital holographic interferometry for biomechanical strain measurements of biological objects, *J. Biomed. Opt.* 19 (12) (2014) 127005.
- [20] M. Estriebeau and P. Magnan, "Fast MTF measurement of CMOS imagers using ISO 12333 slanted-edge methodology," in *Proc.SPIE*, Feb. 2004, vol. 5251.
- [21] E. Buhr, S. Günther-Kohfahl, U. Neitzel, Accuracy of a simple method for deriving the presampled modulation transfer function of a digital radiographic system from an edge image, *Med. Phys.* 30 (9) (Sep. 2003) 2323–2331, <https://doi.org/10.1118/1.1598673>.
- [22] J.W. Goodman, Introduction to Fourier Optics, Second Edition, *Opt. Eng.* (1996), <https://doi.org/10.1117/1.601121>.
- [23] D. Bloch, "Ray Optics extension for Inkscape." <https://inkscape.org/~dbloch/star-ray-optics>.
- [24] T. Shimobaba, T. Ito, Computer Holography: Acceleration Algorithms and Hardware Implementations. (2019), <https://doi.org/10.1201/9780429428005>.
- [25] S. Kinoshita, S. Yoshioka, K. Kawagoe, Mechanisms of structural colour in the Morpho butterfly: cooperation of regularity and irregularity in an iridescent scale, *Proc. R. Soc. Lond. B* 269 (1499) (2002) 1417–1421.
- [26] B. Saleh and M. Teich, *Fundamentals of Photonics, 3rd Edition*. 2019.
- [27] S. Berthier, E. Charron, A. Da Silva, Determination of the cuticle index of the scales of the iridescent butterfly Morpho menelaus, *Opt. Commun.* 228 (4) (2003) 349–356, <https://doi.org/10.1016/j.optcom.2003.10.032>.
- [28] T. Kreis, Handbook of Holographic Interferometry: Optical and Digital Methods, Wiley, 2006.

RESEARCH ARTICLE | JULY 17 2024

Object alignment in spatially multiplexed holograms applied to polarization sensing

Filip Krajinić   ; Petar Atanasijević  ; Peđa Mihailović 



Rev. Sci. Instrum. 95, 073710 (2024)

<https://doi.org/10.1063/5.0203429>



APL Energy

Latest Articles Online!

Read Now



Object alignment in spatially multiplexed holograms applied to polarization sensing

Cite as: Rev. Sci. Instrum. 95, 073710 (2024); doi: 10.1063/5.0203429

Submitted: 13 February 2024 • Accepted: 24 June 2024 •

Published Online: 17 July 2024



View Online



Export Citation



CrossMark

Filip Krajinić,^{1,2,a)}  Petar Atanasijević,¹  and Peđa Mihailović¹ 

AFFILIATIONS

¹University of Belgrade, School of Electrical Engineering, Bulevar kralja Aleksandra 73, 11120 Belgrade, Serbia

²University of Belgrade, Institute of Physics Belgrade, Photonics Center, Pregrevica 118, 11080 Zemun, Belgrade, Serbia

^{a)}Author to whom correspondence should be addressed: filip@ipb.ac.rs

ABSTRACT

The paper presents a new algorithm for object alignment in digital holography with multiple spherical reference waves. The algorithm was applied to polarization sensing with two orthogonally polarized reference waves. A novel holographic setup was built using a diffraction grating to generate two symmetric reference waves, keeping the setup simple and highly adjustable. The angles of rotation of the polarizing elements were calculated with mean absolute errors of 0.71° and 2.96° based on intensity and phase measurements, respectively. The same algorithm can be applied to any digital holographic measurement with multiple spherical reference waves.

Published under an exclusive license by AIP Publishing. <https://doi.org/10.1063/5.0203429>

I. INTRODUCTION

Holography with multiple reference waves contains more information in a single hologram recording compared to its single reference wave counterpart.¹ It is used in multiwavelength holography,²⁻⁵ polarization sensitive holography,^{6,7} and resolution enhancement.⁸ The interference of a single object wave with multiple reference waves results in multiple pairs of object images in the reconstruction plane. Object images must overlap pixel by pixel in the reconstruction plane, to further analyze the amplitudes and phases.

The algorithms performing the alignment of images in the reconstruction can be divided into two categories. The first category crops the objects from the reconstruction and employs a block matching algorithm (BMA) to overlay the images,⁹⁻¹¹ while the second introduces a phase mask during the hologram reconstruction to induce a shift of the objects in the reconstruction plane.^{9,12,13} Thus, the phase mask effectively compensates for the tilts and positions of the reference waves. The former approach is fast, although limited in alignment precision to half of the pixel size in the reconstruction plane. The latter approach provides better results but with increased complexity of the algorithms. The interest in the retrieval of the reference wave's parameters from the hologram reconstruction goes beyond the field of multiple reference wave holography.

It is inspired by research in phase-shifting holography,¹⁴ phase contrast microscopy,¹² and other related fields. However, the used reference wavefronts are usually plane.¹²⁻¹⁴ To retrieve the spherical reference wave's parameters, automated and robust, yet complex algorithms based on speckle displacements and phase derivatives were proposed.^{15,16}

In this paper, we propose a hybrid method for image alignment that uses the simplicity of the BMA and more accurate objects' phase components of the phase mask approach. Our method uses analytical expressions and block matching to estimate the parameters of spherical reference waves. From these parameters, the images can be aligned, and the value of interest can be calculated. To validate the performance of the proposed method, we design a simple and low-cost setup for polarization-sensitive holography with spherical reference waves. We utilize basic polarization varying components as the imaged objects in the experiments, following the previously reported studies.¹⁷⁻¹⁹ For the polarization-sensitive holography, the two reference waves must be of orthogonal polarization.^{7,20} In general, the object wave will interfere with both reference waves, forming two sets of images with two orthogonal polarizations. After the alignment of respective images, the polarization map of the object wave can be determined and expressed using the Jones vector formalism.²¹⁻²³ A state of the art in the field of polarization-sensitive holography is presented in the review article.²⁴

II. METHODOLOGY

Our approach for object matching and alignment was based on the determination of the positions of two spherical reference waves' point sources used for recording the hologram. Its block diagram is shown in Fig. 1. The transmissive object is positioned at the optic axis of the camera, while the reference waves are displaced. This should result in a reconstruction of the object in the center of the reconstruction plane, while the reference wave will be off-axis. To determine the positions of the two spherical reference waves, we first incorrectly assume the reference wave is on the optic axis. That will result in spatially shifting the reconstruction plane so that the reference wave will be in the center and the objects will shift accordingly [Fig. 1(a)]. New object locations, expressed in pixels (m_x, m_y) , are found from this incorrect reconstruction using image correlation [Fig. 1(b)]. One of the objects is selected as a kernel for image correlation. Novelty in the proposed hybrid approach is that these new object locations will be used to determine the positions of the reference waves' point sources in the setup. The knowledge of the reference waves' point source locations allows for exact reconstructions, which will have objects aligned at the center with adequate phase components.

The relation between the position of the spherical reference wave and the pixel position of the maxima in the correlation image is expressed in the following equations, where (x_0, y_0, z_0) represent the location of the reference wave's point source, λ wavelength used to record a hologram, $(\Delta\xi, \Delta\eta)$ pixel size, and N number of pixels:

$$x_0 = -\frac{z_0\lambda}{N\Delta\xi} \left(m_x - \frac{N}{2} \right), \tag{1}$$

$$y_0 = -\frac{z_0\lambda}{N\Delta\eta} \left(m_y - \frac{N}{2} \right). \tag{2}$$

These results are derived from the representation of the hologram reconstruction, Eq. (3), where $p(x, y)$ represents the reconstruction plane, parameter $C_z(x, y)$ was introduced for convenience, $h(\xi, \eta)$ represents the hologram at the camera plane, and z distance between the reconstruction and the camera plane (the detailed derivation can be found in the supplement),

$$p(x, y) = C_z(x, y) \iint_{\xi\eta} h(\xi, \eta) \exp\left(i\frac{\pi}{\lambda} \left(\frac{1}{z} - \frac{1}{z_0} \right) (\xi^2 + \eta^2) \right) \times \exp\left(-i\frac{2\pi}{\lambda z} \left(\xi \left(x - \frac{z}{z_0} x_0 \right) + \eta \left(y - \frac{z}{z_0} y_0 \right) \right) \right) d\xi d\eta, \tag{3}$$

$$C_z(x, y) = \frac{\exp(ikz)}{i\lambda z} \exp\left(i\frac{\pi}{\lambda z} (x^2 + y^2) \right) \exp(-ikz_0) \exp\left(-ik\frac{x_0^2 + y_0^2}{2z_0} \right). \tag{4}$$

The integral in Eq. (3) represents a Fourier transform of the hologram multiplied by the chirp function. If the reference wave is incorrectly simulated $(x_0, y_0) = (0, 0)$, the absence of the additional exponential term within the integral will give the reconstructed image a spatial shift of $(-z/z_0)x_0, -(z/z_0)y_0$, resulting in object reconstruction that is not on the optical axis, contrary to the experimental setup. This spatial shift is equal to the multiplication product of the sampling rate in the reconstruction plane $(\Delta x, \Delta y) = (z\lambda/(N\Delta\xi), z\lambda/(N\Delta\eta))$ and the distance between the position of the object's correlation maxima and the center of the reconstruction $(m_x - N/2, m_y - N/2)$, where N is the number of pixels of the hologram.

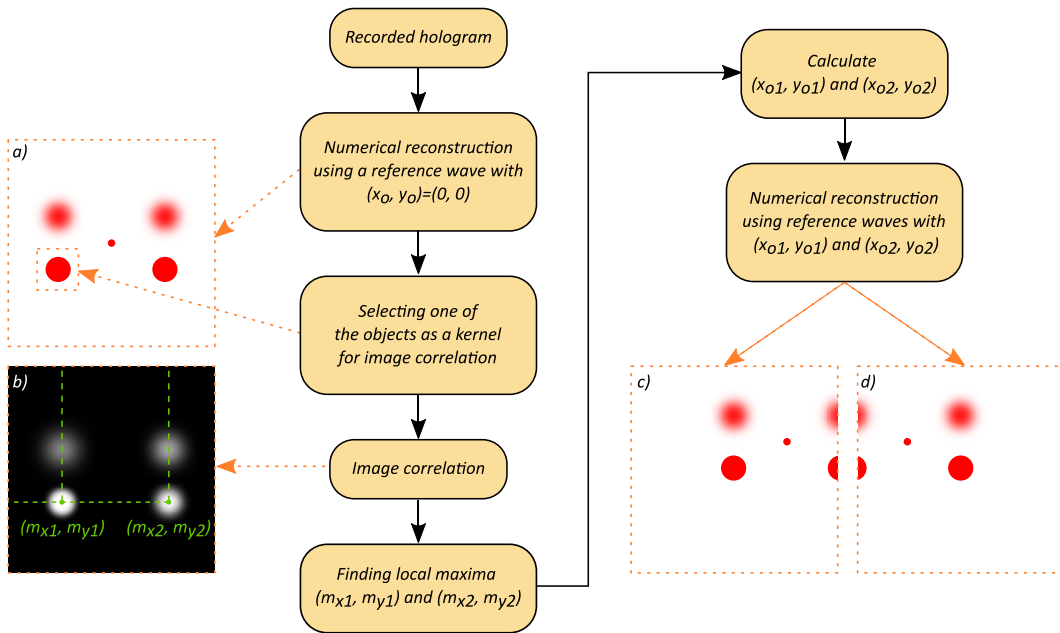


FIG. 1. Block diagram of the algorithm used for object alignment with insets for (a) the hologram reconstruction with incorrectly simulating a reference wave. (b) The result of image correlation. (c) and (d) Hologram reconstruction with the correct first and second reference wave, respectively.

The shift of the reference wave's point source by calculated value of (x_0, y_0) using Eqs. (1) and (2) and separate reconstructions with correct reference waves will align the object with the optic axis as shown in Figs. 1(c) and 1(d), enabling further calculations, i.e., comparison of orthogonal polarization amplitudes and phases.

III. APPLICATION TO POLARIZATION SENSING

In this section, we will explain the holographic polarization sensing setup used for validating our proposed algorithm. The holographic setup with two symmetrical reference waves is depicted in Fig. 2. He-Ne laser (632.8 nm, 5 mW) was used as the light source.

Diffraction grating was used to generate the object wave (zeroth diffraction order) and reference waves (first and first diffraction orders). The grating enables a simple and symmetrical setup keeping the reference waves matched. Diffraction grating bears another benefit. Moreover, by choice of grating fulfillment, the diffraction efficiencies can be adjusted to the optimal power ratio of the object beam (after object) and reference beam (after mirror) of 2:1 if overall attenuation by the object is previously measured.

Reference waves are redirected toward the camera by mirrors and expanded by lenses creating spherical wavefronts. Polarizer sheets were used to set the reference wave polarizations to the linear, mutually orthogonal states.

Using two lens beam expanders (L1 and L2), the object wave is expanded and collimated into a plane wave. To get the maximum sensitivity out of the system, the optical axis of a linear polarizer (P1) following the expander makes a 45° angle with each of the polarizations of the reference waves. If we denote the orientation of the linearly polarized object wave as 0° , then the first and the second reference waves are linearly polarized with orientation of -45° and 45° , respectively. The transparent object modulates the polarization of the object wave, which then creates two orthogonal interference patterns with reference waves. The formed hologram is recorded using a monochromatic digital camera (resolution 5472×3648 , pixel size $2.4 \times 2.4 \mu\text{m}^2$, and 17FPS).

Hologram H recorded by the camera represents the superposition of two holograms H_1 and H_2 made by interfering with the object wave \vec{O} with orthogonal reference waves \vec{R}_1 and \vec{R}_2 . If we note the polarization of the first reference wave with \vec{i}_1 , and the second reference wave with \vec{i}_2 , one can divide the object wave into

two polarization components, which will interfere with the reference wave matching its polarization. In the following equation, we will mathematically express what was previously mentioned:

$$H \propto |\vec{O} + \vec{R}_1 + \vec{R}_2|^2 = |(O_1 + R_1)\vec{i}_1 + (O_2 + R_2)\vec{i}_2|^2 = |(O_1 + R_1)|^2 + |(O_2 + R_2)|^2 \propto H_1 + H_2. \quad (5)$$

The proposed holographic setup contains no beam combiners to limit the size of the recorded object. Thus, the recorded object size is limited to a quarter of the size of the reconstructed image $z\lambda/(2\Delta\xi)$. If P number of reference wave pairs is used to record an object with a dimension of d_0 , the product Pd_0 is limited to be less than the previously established limit $z\lambda/(2\Delta\xi)$. The setup is modular, providing an easy change between macroscopic and microscopic measurements by removing the beam expander in Fig. 2(a) and adding a microscope objective after the object.

To demonstrate the ability of polarization measurement, two experiments were designed. The first experiment measured the orientation of the linear polarization of the object wave using only the intensity images, while the second experiment determined the elliptical polarization state using both the intensity and phase difference images.

The object for the first experiment was designed to provide a linear polarization with constant irradiance. It consisted of a quarter wave plate with a 45° polarizer after it [Fig. 2(b)]. The quarter wave plate and the polarizer are rotated together, yielding equations for the intensities I_x and I_y of the orthogonal polarization components,

$$I = \begin{bmatrix} I_x \\ I_y \end{bmatrix} = \begin{bmatrix} I_0 \cos^2 \Theta \\ I_0 \sin^2 \Theta \end{bmatrix}, \quad (6)$$

where angle Θ is the orientation of the transmission axis of the polarizer (P4) referenced to P1 orientation. The orientation angle Θ is calculated using the following equation:

$$\Theta = \tan^{-1} \left(\sqrt{\frac{I_y}{I_x}} \right). \quad (7)$$

For the case of linear polarization, only the intensity of the two orthogonal components was used since the phase difference is known to be equal to zero or π .

In the second experiment, the object was a rotatable quarter-wave plate, placed in front of a fixed polarizer (P4) covering a part of the object wave and having the same transmission axis as P1. The quarter-wave plate was rotated creating elliptical polarization in the region not covered by P4. For the characterization of elliptical polarization, the phase difference between the electric field components has to be determined. The approach presented by Colomb *et al.*⁷ is used to calculate this phase difference, compensating for the slight mismatch of optical path lengths of the reference waves using P4. The non-zero phase difference $\Delta\phi_{ref}$ in the P4 region of the reconstruction should, thus, be subtracted from the measured phase difference in the quarter-wave plate region $\Delta\phi_m$, leaving the true phase difference of the two orthogonal components $\Delta\phi$, given with the following equation:

$$\Delta\phi = \Delta\phi_m - \Delta\phi_{ref} = \Delta\phi_y - \Delta\phi_x = \tan^{-1} \left(\frac{\cos(2\Theta)}{1 - \cos^2(2\Theta)} \right). \quad (8)$$

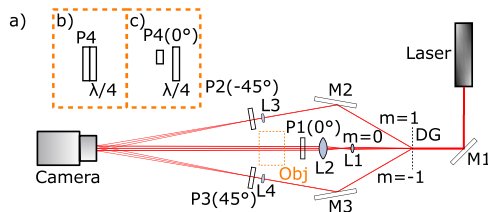


FIG. 2. (a) Holographic setup with two symmetrical reference waves. (b) Inset of the object section in the first experiment. (c) Inset of the object section in the second experiment. (M1, M2, M3—mirrors; L1, L2, L3, L4—lenses; DG—diffraction grating; P1, P2, P3, P4—linear polarizer; Obj—object section; $\lambda/4$ —quarter-wave plate).

Normalized intensities I'_x and I'_y can be expressed with the following equation:

$$I' = \begin{bmatrix} I'_x \\ I'_y \end{bmatrix} = \begin{bmatrix} \frac{1}{2} + \frac{1}{4} \sin(4\Theta) \\ \frac{1}{2} - \frac{1}{4} \sin(4\Theta) \end{bmatrix}. \quad (9)$$

The equations mentioned above can be derived using available the literature.²⁵

IV. RESULTS AND DISCUSSION

For both experiments, the set of holograms covering the object angle range of 0° – 180° with 10° increments were recorded.

The result of the measured orientation of the object's wave linear polarization state is shown in Fig. 3. A median value in the neighborhood of 5×5 pixels in the reconstruction plane was used to obtain the value of a single point on the graph for all the results. The orientation Θ is reduced to the codomain of $[0, \pi/2]$ due to calculating the inverse tangent of non-negative intensity values of I_x and I_y , which can only return values from the first quadrant. The mean absolute error (MAE) in Θ measurement of linear polarization is calculated to be 0.71° .

The results of the hybrid algorithm proposed in this paper are satisfactory when only intensity images are needed for further calculations. When phase images are also needed (the second experiment), the position of the point source must be further adjusted. A slight variation in the position of the point source can make a major difference in the phase of the reconstructed object wave. Error in the position of the point source of a spherical reference wave in the (x, y) plane of this approach cannot be greater than the shift in hologram reconstruction for a single pixel whose value is equal to $z_0\lambda/N$. For more accurate results, the values of (x_0, y_0) should be further adjusted. A major disadvantage of using spherical reference waves to plane reference waves is the distance z_0 must also be adjusted. However, this adjustment can also be automated, i.e., using MAE as a loss metric. Once the setup is calibrated, the measurement results will be valid.

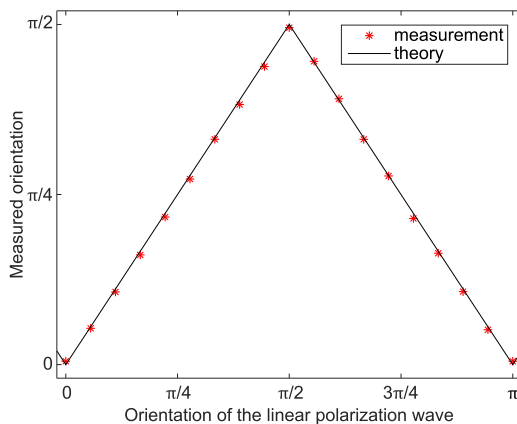


FIG. 3. Comparison between the measured orientation of the object wave's linear polarization state and its theoretical value.

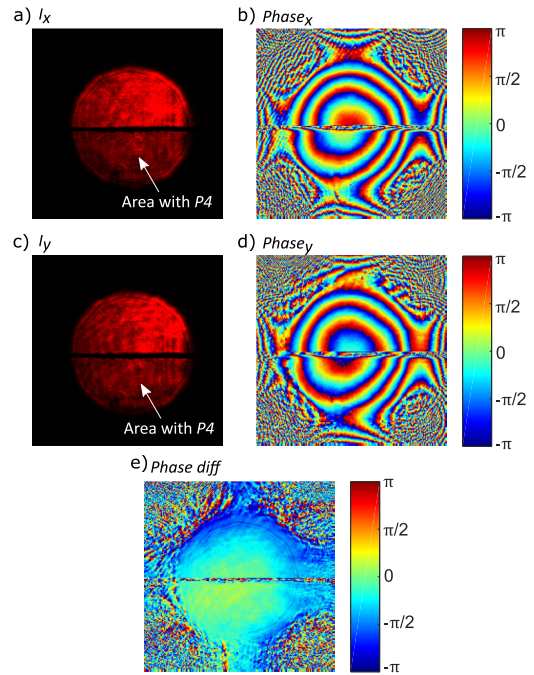


FIG. 4. A part of the reconstruction image of the object's first polarization component (a) intensity distribution and (b) phase distribution. A part of the reconstruction image of the object's second polarization component (c) intensity distribution and (d) phase distribution. (e) Phase difference image of the two orthogonal polarization components.

Figures 4(a)–4(e) show the reconstructed intensity images [Figs. 4(a) and 4(b)], phase images [Figs. 4(c) and 4(d)], and phase difference image [Fig. 4(e)] of the polarization components for the second experiment. Polarizer P4 covers the lower part of the object wave, providing the needed information of $\Delta\phi_{ref}$. The phase difference image is derived from the argument of the division of the two complex hologram reconstructions, rather than subtracting one phase image from another, limiting the influence of noise.

The result of measuring the state of polarization during the second experiment is shown in Fig. 5. The phase difference of the two orthogonal polarization components is shown in Fig. 5(a). Its information is not enough to determine the state of the polarization of the object wave since there are two values of the orientation of the object that can have the same component phase difference. To differentiate between the two states, intensity components I_x and I_y must also be known. The normalized intensity of the two polarization components is shown in Fig. 5(b). Knowing both the intensity and phase difference of the polarization components, the state of polarization is unambiguously determined.

The angle of rotation Θ of the quarter wave plate was calculated from the phase difference. The MAE of the measurement was found to be 2.96° . The larger MAE in the second experiment can be attributed to the systematic error in z_0 parameter determination, affecting only phase, but not intensity images.

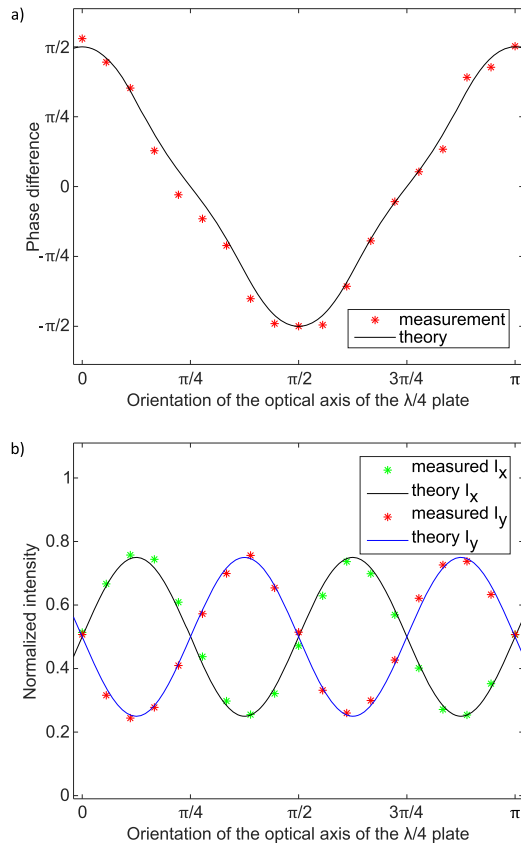


FIG. 5. (a) Relationship between measured phase difference and the orientation of the quarter-wave plate's optical axis. (b) Dependence of the normalized intensities of the two polarization components on the orientation of the quarter-wave plate's optical axis.

V. CONCLUSION

A novel algorithm for object alignment in digital holography with two or more spherical reference waves is presented and experimentally demonstrated. The correct lateral position of the reference point sources is calibrated using a reconstruction with the lateral position on the optic axis, providing a more accurate phase components calculation. The established connection between the object shift in the reconstruction plane and the correct point source position yielded an automated algorithm with accuracy limited by the pixel pitch in the reconstruction plane. To overcome this limit, further adjustments are necessary. To validate the algorithm, a setup for polarization-sensitive holography was devised. The two symmetrical reference waves were created by a diffraction grating keeping the setup simple, low-cost, and interchangeable between microscopic and macroscopic measurements. The setup allows the simultaneous creation of beams with different wavelengths while the optical power matching of the object beam with the reference beams can be done by grating fulfillment. The linear polarizer's and quarter wave plate's optical axis orientation were measured with mean

absolute errors of 0.71° and 2.96° , respectively. The presented algorithm is not limited to reference waves of different polarizations but can be applied to any spatially multiplexed holograms, recorded with spherical reference waves. Applications range from polarization mapping to various compensations and measurements that include multiple wavelengths.

ACKNOWLEDGMENTS

This work was financially supported by the Ministry of Science, Technological Development and Innovation of the Republic of Serbia under Contract No. 451-03-47/2023-01/200103. The authors would like to thank the Palace of Science for the support in the equipment resources.

AUTHOR DECLARATIONS

Conflict of Interest

The authors have no conflicts to disclose.

Author Contributions

Filip Krajinic: Conceptualization (equal); Data curation (equal); Formal analysis (equal); Investigation (equal); Methodology (equal); Software (equal); Validation (equal); Visualization (equal); Writing – original draft (lead); Writing – review & editing (equal). **Petar Atanasijević:** Conceptualization (equal); Data curation (equal); Formal analysis (equal); Investigation (equal); Methodology (equal); Software (equal); Validation (equal); Writing – original draft (equal); Writing – review & editing (equal). **Peda Mihailović:** Conceptualization (equal); Formal analysis (equal); Funding acquisition (equal); Investigation (equal); Methodology (equal); Resources (equal); Supervision (equal); Writing – original draft (equal); Writing – review & editing (equal).

DATA AVAILABILITY

The data that support the findings of this study are available from the corresponding author upon reasonable request.

APPENDIX: DERIVATION OF THE REFERENCE WAVE'S POINT SOURCE LOCATION

To obtain the expression that connects the object's position in the reconstruction image (m_x, m_y) , and the location of the reference wave's point source (x_0, y_0) , we start with the mathematical expression of a spherical reference wave given with the following equation:

$$r(\xi, \eta) = \exp(ik\sqrt{(\xi - x_0)^2 + (\eta - y_0)^2 + z_0^2}), \quad (A1)$$

where k is the wave number and (ξ, η) are the coordinates in the hologram plane, while (x_0, y_0, z_0) represent the location of the reference wave's point source with respect to the optic axis. Considering

that z_0 is sufficiently large, reference waves can be approximated with the following equation:

$$r(\xi, \eta) = \exp(ikz_0) \exp\left(ik \frac{\xi^2 + \eta^2}{2z_0}\right) \times \exp\left(-ik \frac{\xi x_0 + \eta y_0}{z_0}\right) \exp\left(ik \frac{x_0^2 + y_0^2}{2z_0}\right). \quad (\text{A2})$$

The diffraction integral for hologram reconstruction using the approximated reference waves yields the following equations for the field in the reconstruction plane $p(x, y)$:

$$p(x, y) = \frac{\exp(ikz)}{i\lambda z} \exp\left(i \frac{\pi}{\lambda z} (x^2 + y^2)\right) \iint_{\xi\eta} h(\xi, \eta) r^*(\xi, \eta) \times \exp\left(i \frac{\pi}{\lambda z} (\xi^2 + \eta^2)\right) \exp\left(-i \frac{2\pi}{\lambda z} (\xi x + \eta y)\right) d\xi d\eta, \quad (\text{A3})$$

$$p(x, y) = C_z(x, y) \iint_{\xi\eta} h(\xi, \eta) \exp\left(-ik \frac{\xi^2 + \eta^2}{2z_0}\right) \exp\left(ik \frac{\xi x_0 + \eta y_0}{z_0}\right) \times \exp\left(i \frac{\pi}{\lambda z} (\xi^2 + \eta^2)\right) \exp\left(-i \frac{2\pi}{\lambda z} (\xi x + \eta y)\right) d\xi d\eta, \quad (\text{A4})$$

$$C_z(x, y) = \frac{\exp(ikz)}{i\lambda z} \exp\left(i \frac{\pi}{\lambda z} (x^2 + y^2)\right) \exp(-ikz_0) \exp\left(-ik \frac{x_0^2 + y_0^2}{2z_0}\right). \quad (\text{A5})$$

In Eqs. (A3)–(A5), λ is the wavelength of the light source, z represents the distance between the hologram plane and projection plane, $h(\xi, \eta)$ is the hologram's intensity distribution, $r^*(\xi, \eta)$ is the conjugated reference wave, and $C_z(x, y)$ is introduced for convenience. Equation (A4) can be further transformed to a form given with the following equation:

$$p(x, y) = C_z(x, y) \iint_{\xi\eta} h(\xi, \eta) \exp\left(i \frac{\pi}{\lambda} \left(\frac{1}{z} - \frac{1}{z_0}\right) (\xi^2 + \eta^2)\right) \times \exp\left(-i \frac{2\pi}{\lambda z} \left(\xi \left(x - \frac{z}{z_0} x_0\right) + \eta \left(y - \frac{z}{z_0} y_0\right)\right)\right) d\xi d\eta. \quad (\text{A6})$$

This result in the form of a Fourier transform of the product of the hologram and the chirp function is used to derive Eqs. (1) and (2).

REFERENCES

¹T. Kreis, *Handbook of Holographic Interferometry: Optical and Digital Methods* (Wiley, 2006).
²D. G. Abdelsalam, R. Magnusson, and D. Kim, "Single-shot, dual-wavelength digital holography based on polarizing separation," *Appl. Opt.* **50**, 3360 (2011).
³J. Kühn, T. Colomb, F. Montfort, F. Charrière, Y. Emery, E. Cuche, P. Marquet, and C. Depeursinge, "Real-time dual-wavelength digital holographic microscopy with a single hologram acquisition," *Opt. Express* **15**, 7231 (2007).
⁴F. Wang, D. Wang, L. Rong, Y. Wang, and J. Zhao, "Single-shot dual-wavelength in-line and off-axis hybrid digital holography," *Appl. Phys. Lett.* **112**, 091903 (2018).

⁵T. Tahara, Y. Takahashi, T. Komura, T. Kaku, and Y. Arai, "Single-shot multiwavelength digital holography using angular multiplexing and spatial bandwidth enhancement for extending the field of view," *J. Disp. Technol.* **11**, 807 (2015).
⁶L. Han, Z.-J. Cheng, Y. Yang, B.-Y. Wang, Q.-Y. Yue, and C.-S. Guo, "Double-channel angular-multiplexing polarization holography with common-path and off-axis configuration," *Opt. Express* **25**, 21877 (2017).
⁷T. Colomb, P. Dahlgren, D. Beghuin, E. Cuche, P. Marquet, and C. Depeursinge, "Polarization imaging by use of digital holography," *Appl. Opt.* **41**, 27 (2002).
⁸P. Wang, "Improved angular multiplexing method with polarization interference for enhancing the resolution of digital holographic image," *Optik* **131**, 312 (2017).
⁹R. Aylo, G. T. Nehmetallah, and L. Williams, *Analog and Digital Holography with MATLAB* (Society of Photo-Optical Instrumentation Engineers (SPIE), 2015).
¹⁰L. W. G. Nehmetallah and T. Nguyen, "Latest advances in single and multiwavelength digital holography and holographic microscopy," in *Augmented Reality and Its Application* (IntechOpen, 2020).
¹¹L. Williams, P. P. Banerjee, G. Nehmetallah, and S. Praharaaj, "Holographic volume displacement calculations via multiwavelength digital holography," *Appl. Opt.* **53**, 1597 (2014).
¹²E. Cuche, P. Marquet, and C. Depeursinge, "Simultaneous amplitude-contrast and quantitative phase-contrast microscopy by numerical reconstruction of Fresnel off-axis holograms," *Appl. Opt.* **38**, 6994 (1999).
¹³X. Xu, X. Wang, and H. Wang, "Accurate image locating by hologram multiplexing in off-axis digital holography display," *Appl. Sci.* **12**, 1437 (2022).
¹⁴X. Xu, Z. Zhang, Z. Wang, J. Wang, K. Zhan, Y. Jia, and Z. Jiao, "Robust digital holography design with monitoring setup and reference tilt error elimination," *Appl. Opt.* **57**, B205 (2018).
¹⁵D. Khodadad, "Phase-derivative-based estimation of a digital reference wave from a single off-axis digital hologram," *Appl. Opt.* **55**, 1663 (2016).
¹⁶D. Khodadad, P. Bergström, E. Hällstig, and M. Sjö Dahl, "Fast and robust automatic calibration for single-shot dual-wavelength digital holography based on speckle displacements," *Appl. Opt.* **54**, 5003 (2015).
¹⁷D. Khodadad, E. Amer, P. Gren, E. Melander, E. Hällstig, and M. Sjö Dahl, "Single-shot dual-polarization holography: Measurement of the polarization state of a magnetic sample," *Proc. SPIE* **9660**, 96601E (2015).
¹⁸R. Y. Dovhaliuk, "Polarization digital holographic microscopy using low-cost liquid crystal polarization rotators," *Opt. Eng.* **57**, 023104 (2018).
¹⁹M. Yokota, Y. Terui, and I. Yamaguchi, "Analysis of polarization state by digital holography with polarization modulation," *Opt. Rev.* **13**, 405 (2006).
²⁰D. Beghuin, E. Cuche, P. Dahlgren, C. Depeursinge, G. Delacretaz, and R. P. Salathé, "Single acquisition polarisation imaging with digital holography," *Electron. Lett.* **35**, 2053 (1999).
²¹T. Colomb, E. Cuche, F. Montfort, P. Marquet, and C. Depeursinge, "Jones vector imaging by use of digital holography: Simulation and experimentation," *Opt. Commun.* **231**, 137 (2004).
²²X. Liu, B.-Y. Wang, and C.-S. Guo, "One-step jones matrix polarization holography for extraction of spatially resolved jones matrix of polarization-sensitive materials," *Opt. Lett.* **39**, 6170 (2014).
²³X. Liu, Y. Yang, L. Han, and C.-S. Guo, "Fiber-based lensless polarization holography for measuring jones matrix parameters of polarization-sensitive materials," *Opt. Express* **25**, 7288 (2017).
²⁴G. Coppola and M. A. Ferrara, "Polarization-sensitive digital holographic imaging for characterization of microscopic samples: Recent advances and perspectives," *Appl. Sci.* **10**, 4520 (2020).
²⁵S. Huard, *Polarization of Light* (Wiley, 1997).

Thermoelectric temperature control of *Morpho* butterfly wings used for radiation sensing

Petar Atanasijevic¹, Filip Krajinic^{1,2}, Pedja Mihailovic¹, Dejan Pantelic²

(1) School of Electrical Engineering, University of Belgrade, Bulevar kralja Aleksandra 73, 11120, Belgrade, Serbia

(2) Institute of Physics Belgrade, University of Belgrade, Photonics Center, Pregrevica 118, 11080 Zemun, Belgrade, Serbia

Contact: P. Atanasijevic (petarat@etf.bg.ac.rs)

Abstract. Because of their unique optical properties, *Morpho* butterfly wings inspired development of a range of novel sensors in the past decade [1]. Radiation detection proved to be particularly interesting, as it was shown that *Morphos* can detect the infrared part of the spectrum with no need for detector cooling [2,3]. Among the proposed techniques for optical readout of the radiation induced changes, digital holography was the only one to demonstrate image acquisition using a *Morpho didius* wing [4]. In our research, we built upon the principles used for holographic interrogation of the *Morpho* butterfly imaging sensor and developed an experimental setup for thermoelectric (TEC) temperature control of wing's back surface. We used the setup to determine a range of temperatures yielding the optimal sensor holographic response to 5 mW, 632.8 nm laser radiation. The setup used a PSoC 5LP (Programmable System-on-Chip) microcontroller based PID regulator with a Howland current pump [5] for TEC control and LM35 pn junction analog temperature sensor for temperature feedback monitoring, as shown in Figure 1. We investigated both TEC heating and cooling of the wing and observed a change in dynamics of the optomechanical response of the wing scales. A temperature variation of the wing's back surface outside of the range of $\pm 15^\circ\text{C}$ compared to the ambient resulted in a decrease in sensitivity of 20% or more, while no improvement in the frequency bandwidth was observed. The optimal range of wing's back surface temperatures is concluded to be between 15 and 35°C .

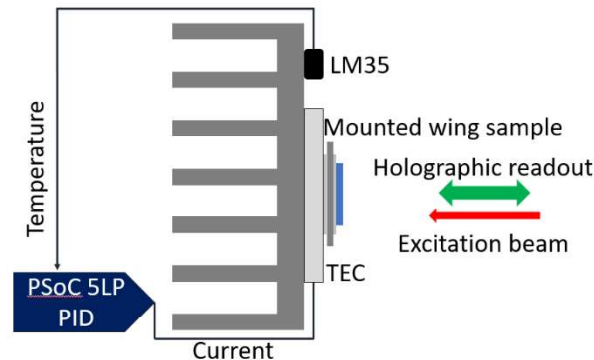


Figure 1. A setup for temperature control of a holographically interrogated *Morpho* wing radiation sensor.

REFERENCES

- [1] Osotsi, M. I. *et al.* Butterfly wing architectures inspire sensor and energy applications. *Natl Sci Rev* **8**, (2021).
- [2] Zhang, F. *et al.* Infrared detection based on localized modification of *Morpho* butterfly wings. *Advanced Materials* (2015)
- [3] Grujić, D. *et al.* Infrared camera on a butterfly's wing. *Opt Express* (2018)
- [4] Atanasijevic, P. *et al.* Characterization of a bioderived imaging sensor based on a *Morpho* butterfly's wing. *Opt Laser Technol* **159**, 108919 (2023).

Optical system for magnetic field spatial distribution measurement using digital holography

Filip Krajinić^{1,2}, Petar Atanasijević¹ and Peđa Mihailović¹

(1) *School of Electrical Engineering, University of Belgrade. Bulevar kralja Aleksandra 73, 11120, Belgrade, Serbia*

(2) *Institute of Physics, University of Belgrade, Photonics Center, Pregrevica 118, 11080, Zemun, Belgrade, Serbia*

Contact: Filip Krajinić (filip@ipb.ac.rs)

Abstract. Spatial distribution of the magnetic field is currently measured with so-called magnetic field cameras, built from the two-dimensional matrix of single point magnetometers, either Hall sensors [1], giant magneto-resistance (GMR) or anisotropic magneto-resistance (AMR) phenomena [2]. Their spatial resolution is limited by the dimensions of the individual sensor element, which is typically in millimeter range. With our research, we present the optical system for measuring the spatial distribution of the magnetic field using the techniques of digital holography to examine the Faraday effect. Faraday crystal in the presence of the magnetic field rotates the polarization of the linearly polarized light. It has been shown that holography with multiple reference waves can be used to measure the state of polarization of the interferometer's object arm [3][4]. We built a holographic setup with two orthogonally polarized reference waves. The laser light is divided into two reference waves and an object wave using a diffraction grating keeping the setup symmetric and simple. We can obtain the intensity of both of the polarization components of the object wave in a single shot. Using the $\Delta/\bar{\epsilon}$ normalization of the polarization component's intensities we can calculate the Faraday rotation which is proportional to the applied magnetic field, keeping the result independent on the laser's power fluctuation. The influence of background light on $\Delta/\bar{\epsilon}$ normalization is inherently eliminated with holographic approach as the magnetic field information is coded in higher spatial frequencies. Sensitivity of the system is determined by the magneto-optical quality of the Faraday crystal. Spatial resolution is set with the camera's properties (dimensions of the sensor chip), laser's wavelength, and the configuration of the optical setup, and can go down to tens of micrometers. Time resolution is limited by the digital camera framerate.

REFERENCES

- [1] H. Phuong, B. Tuan, de Souza-Daw, and T. Hoang, "Magnetic camera for visualizing magnetic fields of home appliances," 2014, doi: 10.1109/CCE.2014.6916732.
- [2] A. B. Suksmono, D. Danudirdjo, A. D. Setiawan, D. Rahmawati, and R. P. Prastio, "A Magnetic Field Camera for Real-Time Subsurface Imaging Applications," *Appl. Sci.*, vol. 11, no. 8, 2021, doi: 10.3390/app11083302.
- [3] T. Colomb, P. Dahlgren, D. Beghuin, E. Cuhe, P. Marquet, and C. Depeursinge, "Polarization imaging by use of digital holography," *Appl. Opt.*, vol. 41, no. 1, pp. 27–37, 2002, doi: 10.1364/AO.41.000027.
- [4] L. Han, Z.-J. Cheng, Y. Yang, B.-Y. Wang, Q.-Y. Yue, and C.-S. Guo, "Double-channel angular-multiplexing polarization holography with common-path and off-axis configuration," *Opt. Express*, vol. 25, no. 18, pp. 21877–21886, Sep. 2017, doi: 10.1364/OE.25.021877.